



Single-atom ruthenium based catalyst for enhanced hydrogen evolution

Dewen Wang^{a,b}, Qun Li^{a,b}, Ce Han^a, Zhicai Xing^{a,*}, Xiurong Yang^{a,b,*}



^a State Key Laboratory of Electroanalytical Chemistry, Changchun Institute of Applied Chemistry, Chinese Academy of Sciences, Changchun 130022, Jilin, China

^b University of Science and Technology of China, Hefei 230026, Anhui, China

ARTICLE INFO

Keywords:

Single-atom
Array-catalyst
Hydrogen evolution reaction
pH-universal
Synergetic catalysis

ABSTRACT

Ruthenium (Ru) as a cheaper alternative to Pt has been studied as a viable alternative for the hydrogen evolution reaction (HER) catalyst, however, no single-atom Ru catalyst has been reported for the HER electrocatalysis. Herein, we design and develop the first type of single-atom Ru based catalyst applied for the HER under pH-universal conditions. This binder-free catalyst consists of single Ru atoms anchored to the surface of MoS₂ nanosheets array supported by a carbon cloth (Ru-MoS₂/CC, Ru in Ru-MoS₂: 0.37 wt%). The abundant dispersed single Ru atoms are highly catalytically active, and the MoS₂ array supported 3D porous structure offers more opportunities for active sites and serves as co-catalysts for synergetic catalysis, with accompanying enhanced the electrical conductivity of this array-catalyst. Remarkably, the Ru-MoS₂/CC exhibits extremely enhanced catalytic activity compared to that of MoS₂/CC and possesses good long-term stability. Density functional theory calculations revealed that the improved catalytic activities stem from the synergistic effect between MoS₂ and single-atom Ru. This discovery holds a great potential to accelerate the large-scale binder-free application of single Ru atoms in industry.

1. Introduction

Electrochemical water splitting, which consists of the hydrogen evolution reaction (HER) and oxygen evolution reaction, is considered as a suitable alternative for the efficient production of hydrogen, playing a key role in overcoming the growing energy crisis and environment issues [1,2]. Recently, despite tremendous efforts had been made for non-noble metal-based catalysts [2,3], but they still demonstrated much inferior performance to that for noble metal-based catalysts and showed higher overpotentials [4,5]. For improving the catalytic activity of noble metal-based catalysts, two general strategies of enhancing the intrinsic activity of each active site (1) and increasing the number of active sites (2) are applied [1]. One attracting approach for achieving strategy (1) is to downsize the noble metal to cluster or even single-atoms for maximizing atom efficiency [6–9]. For example, Cheng et al. synthesized oxidized Pt clusters dispersed on a TiO₂ support (PtO_x in PtO_x/TiO₂: 1.4 wt%) and found that this catalyst has remarkable activity and high stability during the HER when compared with commercial Pt/C [6]. Sun group fabricated single Pt atoms and clusters supported on N-doped graphene nanosheets (NGNs) (Pt in Pt/NGNs: 2.1 wt%) using the atomic layer deposition technique for the HER [7]. Recent works further demonstrated that the photocatalytic efficiency in

hydrogen production of single Pt atoms confined into a metal-organic framework [8] or anchored on g-C₃N₄ [9] were significantly enhanced due to the single Pt atoms can maximize the atom utilization. Another promising approach for realizing strategy (2) is to disperse catalyst on supports [10,11] with high surface area. Qiao et al. reported the first application of iron oxide nanocrystallites (FeO_x) as a support for anchoring isolated single Pt atoms (Pt₁/FeO_x) and this Pt₁/FeO_x catalyst showed excellent stability and high activity towards CO oxidation [10]. Xing group further reported carbon-supported Pt single-atom catalyst for efficient oxygen reduction reaction in fuel cells with high Pt utilization [11]. Although a breakthrough has been achieved in these supported single-atom catalysts [8–12], additional binders are required for applying them on cathodes. Worth mentioning that array-catalysts have recently emerged as an attractive approach for energy applications due to their intrinsic advantages (binder-free nature, 3D porous structure, and large surface area) [2,3]. Zhang et al. synthesized a array-catalyst consisting single Pt atoms on CoP-based nanotube arrays supported by a Ni foam (Pt in PtSA-NT-NF: 1.76 wt%) and the electrocatalytic performances of this binder-free catalyst in neutral media are comparable to those of commercial carbon-supported Pt (Pt/C) [13]. Even major breakthroughs of Pt, which is regarded as 'the Holy Grail' catalyst of the HER, have been achieved, unfortunately, the widespread

* Corresponding authors at: State Key Laboratory of Electroanalytical Chemistry, Changchun Institute of Applied Chemistry, Chinese Academy of Sciences, Changchun 130022, Jilin, China.

E-mail addresses: xingzc@ciac.ac.cn (Z. Xing), xryang@ciac.ac.cn (X. Yang).

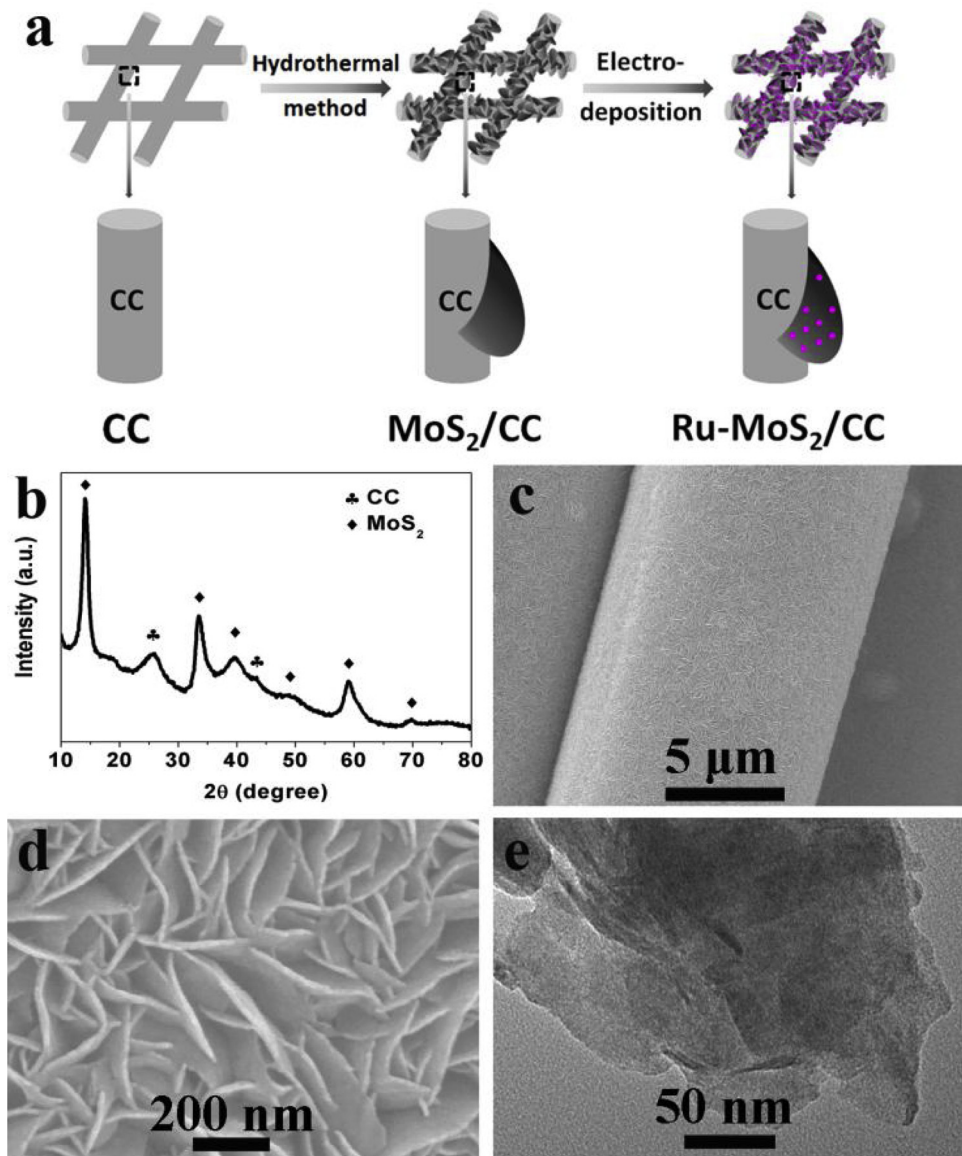


Fig. 1. (a) The fabrication process of Ru-MoS₂/CC array-catalyst. (b) XRD pattern, (c, d) SEM and e) TEM images of Ru-MoS₂/CC.

commercialization of Pt-based catalysts are still hindered due to their scarcity and high cost. Therefore, motivated by these approaches, rational designing array-catalyst at atomic level may explore an attractive class of inexpensive catalysts for alternating Pt catalysts.

Ruthenium (Ru, 42 \$ per oz) as a cheaper alternative to Pt (992 \$ per oz) [14] has evoked special attention as a viable alternative for the HER due to its high similarity to Pt in geometric and electronic structures [14,15]. Jiang et al. prepared Ru nanoparticles modified MoO₂ composite (Ru in Ru-MoO₂: 16.16 wt%) as an active electrocatalyst for the HER under acidic and basic conditions [16]. Baek group further reported a Ru-based catalyst of nitrogenated holey 2D carbon structure (C₂N) supported Ru nanoparticles (Ru in Ru@C₂N: 28.7 wt%) for the HER in acidic and alkaline media [17]. However, up to now, no single-atom Ru based array-catalyst has been reported for the HER electrocatalysis under pH-universal conditions. Herein, we develop that the single Ru atoms as a new form of co-catalyst, which are anchored on MoS₂ nanosheets array supported by a carbon cloth (Ru-MoS₂/CC, Ru in Ru-MoS₂: 0.37 wt%) with high dispersion and stability, can achieve the maximum the efficiency of Ru atoms and synergistically enhance the electrocatalytic activity, representing a new and highly efficient catalytic system for pH-universal hydrogen evolution. In alkaline

condition, Ru-MoS₂/CC array-catalyst as a binder-free cathode exhibits a low overpotential (η) of 171 mV for the HER current density (j_{HER}) of 100 mA cm⁻², which is only 5 mV larger than that of commercial carbon-supported Pt (Pt in Pt/C, 20 wt%; Pt/C was immobilized on CC and denoted as Pt/C/CC) catalyst. However, when $j_{\text{HER}} > 145$ mA cm⁻², the η values of Ru-MoS₂/CC are prominently smaller and thus better than those of Pt/C/CC. More importantly, Ru-MoS₂/CC shows much enhanced activity for the HER in comparison with that of MoS₂/CC in acidic and neutral conditions. Additionally, Ru-MoS₂/CC maintains its activity during long-term chronoamperometric test at pH-universal conditions. Our theoretical calculations based on density functional theory (DFT) further demonstrate that the introduction of single-atom Ru on MoS₂ surface can significantly decrease the Gibbs free energy of hydrogen adsorption (ΔG_{H}), thereby leading to substantially enhanced HER performance. This work provides a universal strategy for developing large-scale array-catalysts with highly-dispersed single-atoms for the sustainable production of fuels and chemical.

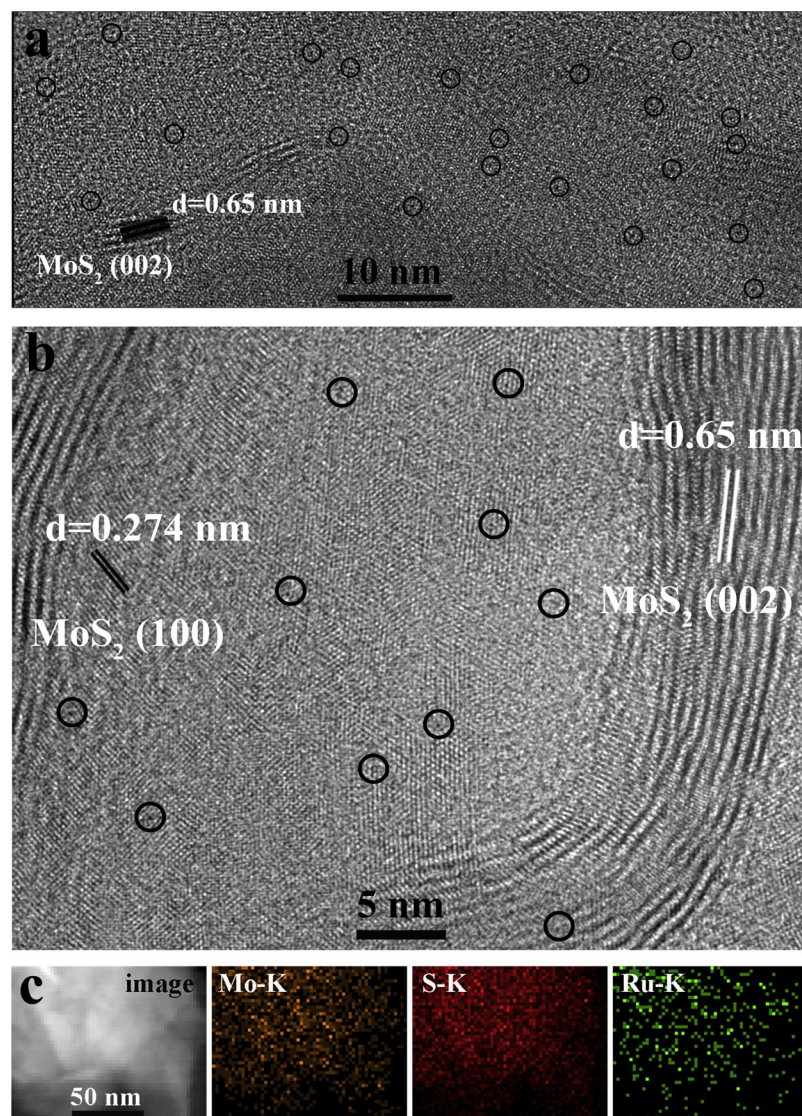


Fig. 2. (a, b) The atomic-resolution TEM images of Ru-MoS₂ (Single Ru atoms were marked by circles). (c) STEM image and EDX elemental mapping images of Mo, S, and Ru for Ru-MoS₂ nanosheet.

2. Experimental section

2.1. Materials

CC (WOS 1002) was purchased from CeTech Co. Ltd., China. Na₂MoO₄·2H₂O, thiourea, ruthenium(III) chloride hydrate, and Nafion (5 wt%) were purchased from Sigma-Aldrich. NaH₂PO₄ and Na₂HPO₄ were purchased from Beijing Chemical Corp. (China). H₂SO₄ and KOH were purchased from Aladdin Ltd. (Shanghai, China). Pt/C (20 wt % Pt on carbon black) was bought from Alfa Aesar. All chemicals were used as received without further purification. The water used throughout all experiments was purified through a Millipore system.

2.2. Preparation of Ru-MoS₂/CC

Typically, MoS₂/CC (MoS₂ loading: 12.40 mg cm⁻²) was prepared from previously reported work [18]. Then, the electrodeposition was carried out in a three-electrode cell using MoS₂/CC as the working electrode, a graphite plate as the counter electrode, and a saturated calomel electrode (SCE) as the reference electrode. Atomically Ru was electrodeposited by cycling MoS₂/CC (1 cm²) substrate from -0.5 to 0.4 V vs. SCE at the sweep rate of 20 mV s⁻¹ in the electrolyte (20 mL

containing RuCl₃ (1 mmol L⁻¹) and H₂SO₄ (0.1 mol L⁻¹) for 20 cycles. All these procedures were carried out at 25 °C. After deposition, the Ru-MoS₂/CC was removed from the cell and rinsed with deionized water several times and dried by nitrogen flow. The loading for Ru on MoS₂/CC was determined to be about 46 µg cm⁻² by quantitatively measuring the concentration difference of Ru in the electrolyte through inductively coupled plasma mass spectrometry technique for multiple identically-prepared samples before and after electrodeposition of Ru. The reference sample, Ru/CC was prepared through the similar method to Ru-MoS₂/CC using the CC as the working electrode.

2.3. Temperature-programmed reduction (TPR) measurements

TPR measurements of the self-supported catalyst systems were determined by static H₂ chemisorption with an Autosorb 1C from Quantachrome. For analysis, roughly 90 mg of catalysts were placed in the sample cell, purged with He gas at 300 °C for 0.5 h, and cooled down to 25 °C under the same gas flow. Then, the 10% H₂/He (50 mL min⁻¹) was admitted into the reactor and the flow was stabilized for 30 min before increasing the temperature to 600 °C at a heating rate of 10 °C min⁻¹.

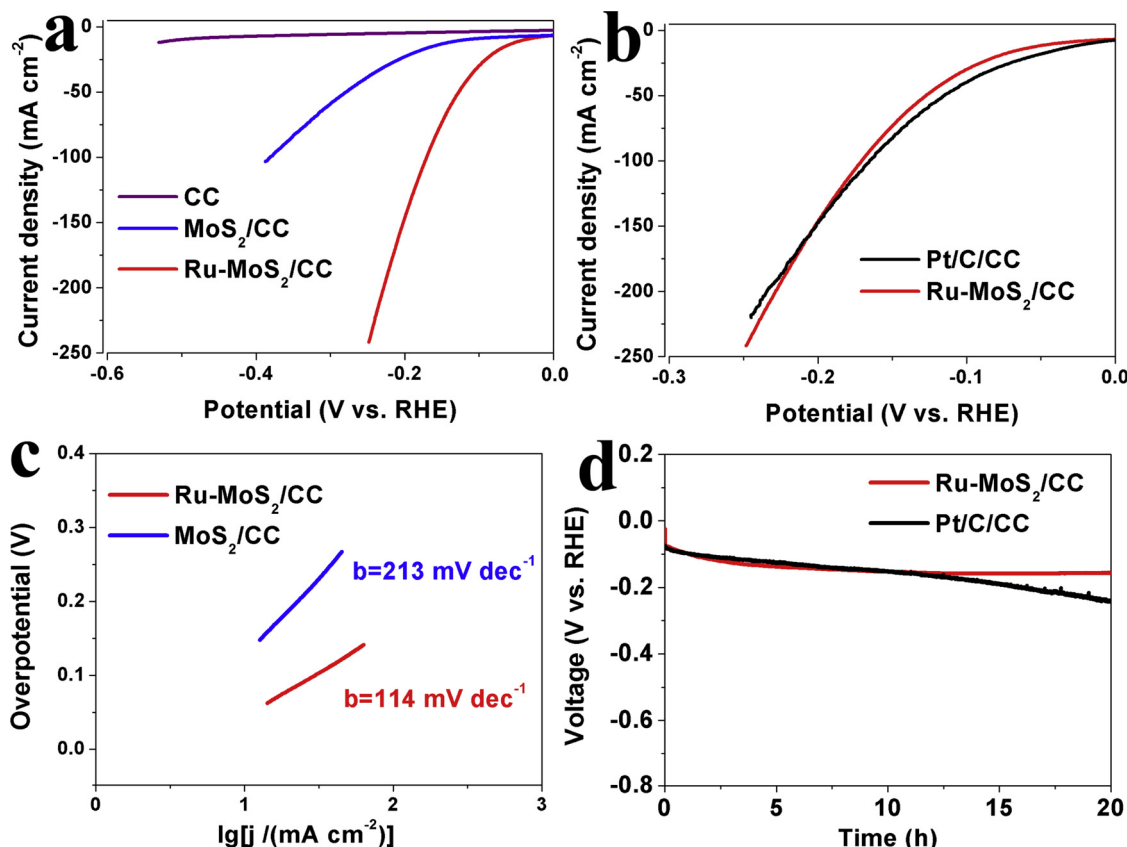


Fig. 3. (a) Polarization curves of bare CC, MoS₂/CC, and Ru-MoS₂/CC (Ru loading: 46 $\mu\text{g cm}^{-2}$) in 1.0 M KOH solution with a scan rate of 5 mV s^{-1} . (b) Polarization curves of Ru-MoS₂/CC and Pt/C/CC (Pt/C loading: 0.23 mg cm^{-2} ; Pt loading: 46 $\mu\text{g cm}^{-2}$) in 1.0 M KOH solution with a scan rate of 5 mV s^{-1} . (c) The Tafel plots of MoS₂/CC and Ru-MoS₂/CC. (d) The chronopotentiometric measurements of long-term stability for Ru-MoS₂/CC and Pt/C/CC at 10 mA cm^{-2} for 20 h.

2.4. Characterizations

Powder XRD data were acquired on a RigakuD/MAX 2550 diffractometer with Cu K α radiation ($\lambda = 1.5418 \text{ \AA}$). SEM measurements were carried out on a XL30 ESEM FEG microscope at an accelerating voltage of 20 kV. The BET surface area and pore size were measured on a Quantachrome NOVA 1000 system at liquid N₂ temperature. TEM measurements were performed on a HITACHI H-8100 electron microscopy (Hitachi, Tokyo, Japan) with an accelerating voltage of 200 kV. Atomic-resolution TEM images were conducted using an FEI TITAN3 G2 60-300S/TEM operating at 300 kV with a spherical aberration (Cs) corrector. XPS measurements were performed on an ESCALABMK II X-ray photoelectron spectrometer using Mg as the exciting source.

2.5. Electrochemical measurements

All the electrochemical measurements were conducted using a CHI660E potentiostat (CH Instruments, China) in a typical three-electrode setup, using a piece of freshly made Ru-MoS₂/CC as the working electrode, a graphite rod as the counter electrode and a saturated calomel electrode (SCE) as the reference electrode. Commercial Pt/C loaded on CC were prepared for comparison. Pt/C powder (3 mg) was firstly dispersed into 990 μL of water/ethanol (v/v = 1:1) solvent containing 10 μL of 5 wt% Nafion and sonicated for 30 min. Then, 19.2 μL of the Pt/C ink was loaded on CC (0.25 cm^{-2}) with Pt loading of 46 $\mu\text{g cm}^{-2}$ (Pt/C loading: 0.23 mg cm^{-2}) for activity and stability test. Prior to measurement, a resistance test was made and the iR compensation was applied to all initial data for further analysis. EIS measurements were carried out in the frequency range of 100 kHz–0.01 Hz. In all measurements, the SCE reference electrode was calibrated with respect to RHE. In 1.0 M KOH, $E(\text{RHE}) = E(\text{SCE}) + 1.067 \text{ V}$. In 1.0 M

PBS, $E(\text{RHE}) = E(\text{SCE}) + 0.655 \text{ V}$. In 0.5 M H₂SO₄, $E(\text{RHE}) = E(\text{SCE}) + 0.280 \text{ V}$. LSV curves were conducted in electrolyte with scan rate of 5 mV s^{-1} without any activation. All the potentials reported in our work were expressed vs. the RHE.

2.6. Turnover frequency (TOF) calculation

The TOF (s^{-1}) was calculated following equation:

$$\text{TOF} = I/2nF$$

I: Current (A) during the LSV measurement.

F: Faraday constant (C/mol).

n: Number of active sites (mol), which obtained from previous reported method [19]. Briefly, the CV measurements of freshly prepared MoS₂/CC and Ru-MoS₂/CC electrode were carried out in PBS electrolyte (pH 7). Assuming one electron redox process, the number of active sites (n) of these electrode were calculated from the following equation: $n = Q/2F$, where F and Q are the Faraday constant and the whole charge of CV curve, respectively.

The factor 1/2 arrives by taking into account that two electrons are required to form one hydrogen molecule from two protons.

2.7. Computational section

The first principles calculations in the framework of density functional theory, including structural and electronic performances, were carried out based on the Cambridge Sequential Total Energy Package known as CASTEP [20]. The exchange–correlation functional under the generalized gradient approximation (GGA) [21] with norm-conserving pseudopotentials and Perdew–Burke–Ernzerhof functional was adopted to describe the electron–electron interaction [22]. An energy cutoff of

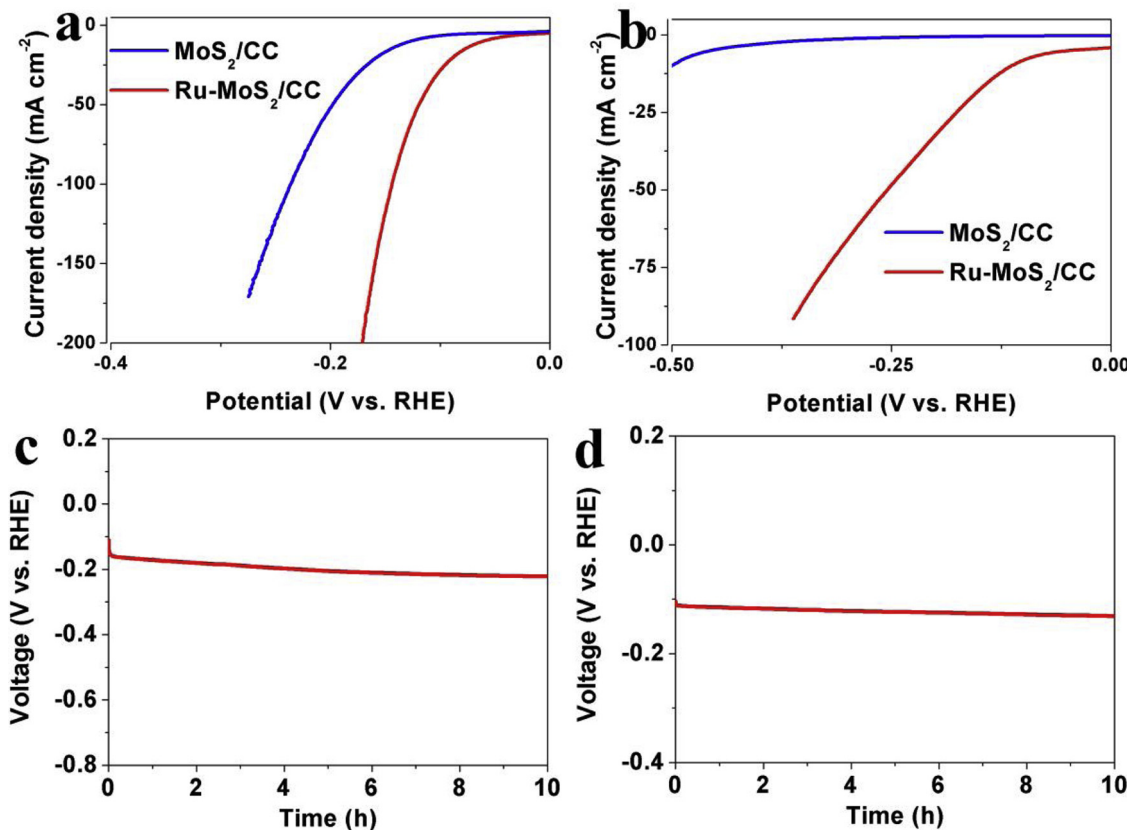


Fig. 4. Polarization curves for MoS₂/CC and Ru-MoS₂/CC in (a) 0.5 M H₂SO₄ and (b) 1 M PBS solution with a scan rate of 5 mV s⁻¹. The chronopotentiometric measurements of long-term stability of Ru-MoS₂/CC in (c) 0.5 M H₂SO₄ and (d) 1 M PBS solution at 10 mA cm⁻² for 10 h.

720 eV was used and a k-point sampling set of $4 \times 4 \times 1$ were tested to be converged. A force tolerance of 0.01 eV \AA^{-1} , energy tolerance of $5.0 \times 10^{-7} \text{ eV}$ per atom and maximum displacement of $5.0 \times 10^{-4} \text{ \AA}$ were considered. The bottom three atomic layers are fixed and the top three atomic layers are relaxed. The vacuum space along the z direction is set to be 15 Å, and the surface of 2H-MoS₂ (100), 2H-MoS₂ (100) + Ru, far S site and near S site on Ru-MoS₂ with lattice constants of $a=b < 12.600 \text{ \AA}$ [17], which is enough to avoid interaction between the two neighboring images. Then, the H atom has been absorbed on the surface of them.

Adsorption energy ΔE of H atom on the surface of substrates was defined as:

$$\Delta E = E_{*H} - (E_{*} + E_H) \quad (1)$$

where $*H$ and $*$ denote the adsorption of H atom on substrates and the bare substrates, E_H denotes the half of energy of H₂.

Free energy change ΔG of the reaction was calculated as the difference between the free energies of the initial and final states as shown below:

$$\Delta G = \Delta E + \Delta ZPE - T\Delta S \quad (2)$$

where E is the calculated energy by DFT, ZPE is the zero point energy, S denotes the entropy, The value of $(\Delta ZPE - T\Delta S)$ is 0.24 eV [23], $\Delta G = \Delta E + 0.28 \text{ eV}$.

3. Results

Single-atom Ru based array-catalyst was successfully developed by electrodeposition of Ru on the surface of MoS₂ nanosheets array which obtained by hydrothermal synthesis method, as shown in Fig. 1a. It is worth mentioning that the optical image of a piece of sample show that the array-catalyst has centimeter-scale dimension (2 cm × 4 cm) (Fig.

S1) which determined by the volumes of Teflon-lined stainless steel autoclave and the three-electrode cell, and thus the single-atom Ru based array-catalyst is scalable. The X-ray diffraction (XRD) pattern (Fig. S2a) and X-ray photoelectron spectroscopy (XPS) spectra (Fig. S3) confirmed that the successful synthesis of MoS₂. The scanning electron microscopy (SEM) images (Fig. S2b and S2c) showed that the surface of CC was vertically and densely covered by aligned MoS₂ nanosheets with the thickness ranged from 12 to 21 nm. This 3D array structure of MoS₂ possessed large Brunauer-Emmett-Teller (BET) surface area of $38.3 \text{ m}^2 \text{ g}^{-1}$ and average pore size of 6.4 nm, respectively (Fig. S4). The XRD pattern of Ru-MoS₂/CC shows that the Ru crystal phases cannot be detected (Fig. 1b) due to the low percentage of Ru in Ru-MoS₂ (about 0.37 wt%). The SEM and transmission electron microscopy (TEM) images of Ru-MoS₂/CC do not exhibit observable particles (Fig. 1c–e), which is probably owing to the resolution limit of TEM. Delightedly, the existence of abundant single Ru atoms can be evidenced by atomic-resolution TEM with a spherical aberration (Cs) corrector (Fig. 2). Fig. 2a showed that Ru-MoS₂ consists of nanosheets with a layer distance of 0.65 nm, corresponding to the (002) plane of MoS₂ [24,25]. The dark spots marked with circles are belong to single Ru atoms with ultra-small sizes between 0.1 and 0.2 nm uniformly dispersed over MoS₂ nanosheet (Fig. 2a and b). The XPS spectra (Fig. S5) show the presence of Mo, S, and Ru elements, while the peaks at about 462.0 and 484.3 eV belong to Ru 3p_{3/2} and Ru 3p_{1/2} of Ru (0) (Fig. S5c) [17]. Homogeneous distribution of single Ru atoms over the MoS₂ nanosheet is further corroborated by scanning TEM (STEM) coupled energy dispersive X-ray (EDX) element mapping images (Fig. 2c). The above results demonstrate that single Ru atoms are successfully electrodeposited over MoS₂ nanosheets array.

The HER catalytic activity of Ru-MoS₂/CC was firstly studied in alkaline solution (N₂-saturated 1.0 M KOH) using a typical three electrode system and the results were shown in Fig. 4. All the

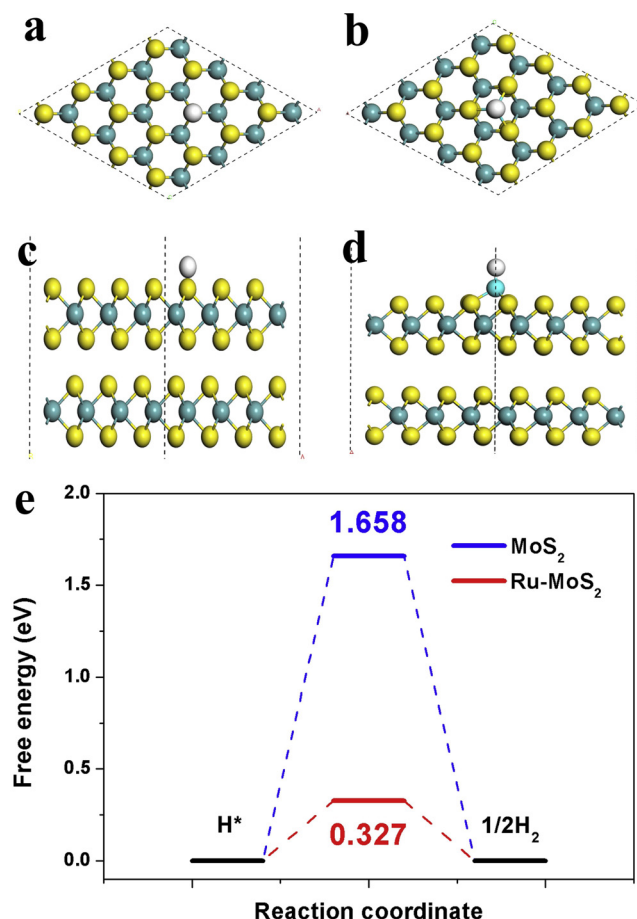


Fig. 5. The optimized structural representations for hydrogen adsorption on (a, c) MoS₂ (100) and (b, d) Ru-MoS₂ (100). (a, b): Top-view, (c, d): side-view. (e) HER free energy change for MoS₂ (100) and Ru-MoS₂ (100).

electrochemical data were exhibited with *iR*-drop compensation based on electrochemical impedance spectroscopy (EIS) measurements [26–28]. The HER activities of MoS₂/CC and bare CC were also measured for comparative purpose. According to Figs. 3a and S6, the η values for MoS₂/CC, Ru/CC, and Ru-MoS₂/CC at $j_{\text{HER}} = 10 \text{ mA cm}^{-2}$ are 300, 121, and 41 mV, respectively, indicating that the introduction of single Ru atoms can contribute to the HER performance of Ru-MoS₂/CC. As control, bare CC showed poor HER activity. Note that, the η value for Ru-MoS₂/CC (171 mV) at $j_{\text{HER}} = 100 \text{ mA cm}^{-2}$ was only 5 mV larger than that (166 mV) for Pt/C/CC (Fig. 3b). More importantly, Ru-MoS₂/CC exhibits much smaller η values than those for Pt/C when $j_{\text{HER}} > 145 \text{ mA cm}^{-2}$, indicating that the electrocatalytic performance of Ru-MoS₂/CC at high current densities was better than that of Pt/C/CC (Fig. 3b). The extracted Tafel slopes from linear portion of the Tafel plots were applied to investigate the HER kinetics of these catalysts (Fig. 3c). The Tafel slope of Ru-MoS₂/CC in the overpotential interval between 0.05 and 0.3 V is 114 mV dec⁻¹, which was much smaller than that of MoS₂/CC (213 mV dec⁻¹), indicating Ru-MoS₂/CC had much enhanced kinetic radical step for HER. Additionally, EIS measurements showed that Ru-MoS₂/CC had a much lower electronic transport and mass transport resistance than that of MoS₂/CC (Fig. S7), and thus markedly accelerate the HER kinetics [29,30].

The chronopotentiometric measurements of HER on Ru-MoS₂/CC and Pt/C/CC were carried out at 10 mA cm^{-2} for 20 h (Fig. 3d) for further evaluating their stabilities. Fig. 3d show that Ru-MoS₂/CC can maintain a relatively stable HER performance for 20 h, whereas the corresponding performance of Pt/C/CC decreased gradually [17], demonstrating the high durability of Ru-MoS₂/CC. The surface

morphology of Ru-MoS₂/CC after the constant reaction for 20 h was well-maintained as shown in Fig. S8 and single Ru atoms can be observed in Fig. S9, further confirming their presence after constant reaction. After constant HER reaction, the XPS spectra indicated that the characteristic peaks of Mo 3d, S 2p, and Ru 3p are almost same to that of Ru-MoS₂/CC before HER test, as shown in Fig. S10. Both SEM and XPS results verified that Ru-MoS₂/CC had highly structural stability during long-term electrochemical processes.

The HER performances of Ru-MoS₂/CC and MoS₂/CC were further studied in 0.5 M H₂SO₄ and 1 M phosphate buffer solution (PBS) solutions. Remarkably, the values for Ru-MoS₂/CC at $j_{\text{HER}} = 10 \text{ mA cm}^{-2}$ are 61 and 114 mV in acidic and neutral condition, respectively, while those for MoS₂/CC were much larger (Fig. 4a and b). Moreover, Ru-MoS₂/CC showed excellent durability with negligible degradation in acidic and neutral solutions (Fig. 4c and d), demonstrating their high stability of Ru-MoS₂/CC, which was confirmed by its stable structure (Figs. S11 and S12) and electrocatalytic kinetics (Figs. S13 and S14). Furthermore, Ru-MoS₂/CC exhibited smaller charge transfer resistance than those for MoS₂/CC in both acidic and neutral condition during the HER process, suggesting that the efficient HER kinetics occurred at the interface between Ru-MoS₂/CC and the electrolyte (Figs. S13 and S14).

4. Discussion

On basis of the above characterizations results, it is well concluded that the enhanced hydrogen evolution activity of Ru-MoS₂/CC is close related to the unique structure of MoS₂ nanosheets array and single Ru atoms. To clarify the influence of the electrochemically active surface areas (ECSAs) on the electrocatalytic HER activity, the ECSAs of MoS₂/CC and Ru-MoS₂/CC catalysts were firstly studied by extracting their double-layer capacitances (C_{dl}) from measured cyclic voltammetry (Fig. S15) [31]. For comparison, the C_{dl} of MoS₂/CC was approximately 56 m F cm⁻² (Fig. S15c). However, the Ru-MoS₂/CC showed higher C_{dl} value of 65 m F cm⁻², implying a higher surface area and exposing more active sites, which is beneficial in increasing the HER activity. Then, the estimation of TOF for each active site of MoS₂/CC and Ru-MoS₂/CC were further performed for revealing their intrinsic catalytic activity [19]. As shown in Fig. S16, Ru-MoS₂/CC needs an overpotential of 169 mV to achieve a TOF of 0.2 s⁻¹, which was much smaller than that (377 mV) of MoS₂/CC, indicating superior kinetic activity of Ru-MoS₂/CC. To further investigate the role of Ru in electrochemical HER, the Ru-MoS₂/CC with different content of Ru were prepared. The polarization curves for Ru-MoS₂/CC with electrodeposition of Ru on MoS₂/CC at different duty cycles were shown in Fig. S17a, which showed that the electrocatalytic activity increases firstly and then decreases with the duty cycles increasing from 15 to 25 cycles. The Ru-MoS₂/CC showed the highest electrocatalytic activity when the duty cycle is fixed at 20 cycles, suggesting the duty cycles of 20 is the optimal condition in our system. EIS analysis confirmed that Ru-MoS₂/CC of 20 cycles has the lowest impedance among these three samples (Fig. S17b). It is worth mention that some Ru clusters will be found in the TEM image (Fig. S18) for electrodeposition of Ru on MoS₂/CC at 25 cycles, which probably led to the slightly decrease in catalytic activity. Furthermore, the TOF values of Ru on MoS₂/CC at different duty cycles (Fig. S19) further suggesting Ru-MoS₂/CC of 20 cycles is the optimal catalytic system.

For obtaining the fundamental insight into the role of single-atom Ru on MoS₂, the TPR experiments of MoS₂/CC and Ru-MoS₂/CC were performed. The TPR profile of MoS₂/CC exhibited one sharp peak at a higher temperature of 375 °C (Fig. S20a) which could be assigned to the bulk reduction of MoS₂ phase [32]. However, when Ru was introduced on the surface of MoS₂ catalyst, the temperature reduction peak significantly shifted from 375 to 262 °C (Fig. S20b), explaining the reduction behavior of MoS₂/CC was greatly improved by Ru promotion due to the possible interaction between Ru and MoS₂ support [33,34]. The small peaks noted on the Ru-MoS₂/CC at lower temperature of 150

and 179 °C which were probably due to the reduction of undecomposed RuCl_3 [33,35], whereas the peaks at high temperature of 324 and 370 °C were probably due to the bulk reduction of MoS_2 phase. It is worth mention that the amount of H_2 consumption on $\text{Ru}-\text{MoS}_2/\text{CC}$ was significantly lower than that required for MoS_2/CC , which was probably due to the introduction of single Ru atoms and strong interactoin between Ru and MoS_2 [33]. Finally, the DFT was utilized to calculate the chemisorption free energies of hydrogen (ΔG_H) on MoS_2 and $\text{Ru}-\text{MoS}_2$ (Fig. 5) for understanding the synergistic effects originating from MoS_2 and single Ru atoms (Figs. S21 and 5 a–d). Generally, a good catalyst should show a optimal ΔG_H value close to 0 eV, which is a key descriptor of the catalytic activity [14]. The computational studies demonstrate that MoS_2 (100) has a large ΔG_H value of 1.658 eV, which is similar to that reported previously [36]. When single-atom Ru was brought into contact with MoS_2 surface, the ΔG_H value is efficiently decreased to 0.327 eV, indicating significant improvement in HER activity (Fig. 5e). Note that the ΔG_H values for far S site (1.571 eV) and near S site (1.022 eV) on $\text{Ru}-\text{MoS}_2$ surface (Fig. S22) are much larger than that for $\text{Ru}-\text{MoS}_2$ (Fig. S22e), further suggesting the constructed interface between MoS_2 and single-atom Ru is the major active sites. Therefore, when compared with that of MoS_2/CC , the significantly enhanced HER activity of $\text{Ru}-\text{MoS}_2/\text{CC}$ can be attributed to the following reasons: (1) The intimate contact between $\text{Ru}-\text{MoS}_2$ array and CC (Fig. 1c) enabled robust adhesion and facilitated electron transport [37]; (2) The hierarchical pathways between neighboring nanosheet array (Fig. 1d) made more active material exposed to the electrolyte and thus allowed easier contact between them; (3) The array structure of MoS_2 nanosheets was not only used as a 3D support [18] for electrodeposition of Ru, but also served as a synergistic co-catalyst [38,39] for enhanced hydrogen evolution; (4) The electrodeposition of Ru increased the conductivity (Fig. S7) of MoS_2/CC and favored fast electron transport along the $\text{Ru}-\text{MoS}_2$ sheet [26], thus highlighting the synergistic effect between MoS_2 sheet and single-atom Ru (Fig. 2) [17,40–42]; (5) The anchored individual single Ru atoms realized the maximized atomic efficiency [12].

5. Conclusions

In summary, we successfully developed a single-atom Ru based catalyst based on our theoretical predictions, which consists single Ru atoms on MoS_2 nanosheets array supported by a CC, using the facile electrodeposition technique. This scalable array-catalyst is the first type of single Ru atoms used for the HER electrocatalysis and it can be directly applied as binder-free cathodes for pH-universal hydrogen evolution. Under alkaline condition, $\text{Ru}-\text{MoS}_2/\text{CC}$ exhibits $\eta = 171$ mV for $j_{\text{HER}} = 100 \text{ mA cm}^{-2}$ which is comparable to that (166 mV) of Pt/C/CC , however, its η values become smaller and thus better than those of Pt/C/CC at $j_{\text{HER}} > 145 \text{ mA cm}^{-2}$. In addition, this array-catalyst also functions as an efficient 3D cathode for HER under acidic and neutral medias. More strikingly, $\text{Ru}-\text{MoS}_2/\text{CC}$ shows much better durability than those for Pt/C/CC under pH-universal conditions. Our density functional theory calculations and experimental results reasonably validate that the synergistic effect between MoS_2 and single-atom Ru is accountable for the outstanding HER catalytic activity. This proof-of-concept study introduces single Ru atoms as a binder-free, scalable, and HER co-catalyst for future energy applications.

Acknowledgments

This work was supported by the National Natural Science Foundation of China (No. 21603215, 21435005, and 21627808), Key Research Program of Frontier Sciences, Chinese Academy of Sciences (No. QYZDY-SSW-SLH019) and the Development Project of Science and Technology of Jilin Province (No. 20180520146JH).

Appendix A. Supplementary data

Supplementary material related to this article can be found, in the online version, at doi:<https://doi.org/10.1016/j.apcatb.2019.02.059>.

References

- [1] Z.W. Seh, J. Kibsgaard, C.F. Dickens, I. Chorkendorff, J.K. Nørskov, T.F. Jaramillo, *Science* 355 (2017) eaad4998.
- [2] X. Zou, Y. Zhang, *Chem. Soc. Rev.* 44 (2015) 5148–5180.
- [3] J. Wang, W. Cui, Q. Liu, Z. Xing, A.M. Asiri, X. Sun, *Adv. Mater.* 28 (2016) 215–230.
- [4] Y. Zheng, Y. Jiao, Y. Zhu, L. Li, Y. Han, Y. Chen, A. Du, M. Jaroniec, S. Qiao, *Nat. Commun.* 5 (2014) 3783.
- [5] S. Cobo, J. Heidkamp, P. Jacques, J. Fize, V. Fourmond, L. Guetaz, B. Jousselme, V. Lvanova, H. Dau, S. Palacin, M. Fontecave, V. Artero, *Nat. Mater.* 1 (2012) 802–807.
- [6] X. Cheng, Y. Li, L. Zheng, Y. Yan, Y. Zhang, G. Chen, S. Sun, J. Zhang, *Energy Environ. Sci.* 10 (2017) 2450–2458.
- [7] N. Cheng, S. Stambula, D. Wang, M.N. Banis, J. Liu, A. Riese, B. Xiao, R. Li, T. Sham, L. Liu, G.A. Botton, X. Sun, *Nat. Commun.* 7 (2016) 13638.
- [8] X. Fang, Q. Shang, Y. Wang, L. Jiao, T. Yao, Y. Li, Q. Zhang, Y. Luo, H. Jiang, *Adv. Mater.* 30 (2018) 1705112.
- [9] X. Li, W. Bi, L. Zhang, S. Tao, W. Chu, Q. Zhang, Y. Luo, C. Wu, Y. Xie, *Adv. Mater.* 28 (2016) 2427–2431.
- [10] B. Qiao, A. Wang, X. Yang, L.F. Allard, Z. Jiang, T. Cui, J. Liu, J. Li, T. Zhang, *Nat. Chem.* 3 (2011) 634–641.
- [11] J. Liu, M. Jiao, L. Lu, H.M. Barkholtz, Y. Li, Y. Wang, L. Jiang, Z. Wu, D. Liu, L. Zhuang, C. Ma, J. Zeng, B. Zhang, D. Su, P. Song, W. Xing, W. Xu, Y. Wang, Z. Jiang, G. Sun, *Nat. Commun.* 8 (2017) 15938.
- [12] X. Yang, A. Wang, B. Qiao, J. Li, J. Liu, T. Zhang, *Acc. Chem. Res.* 46 (2013) 1740–1748.
- [13] L. Zhang, L. Han, H. Liu, X. Liu, J. Luo, *Angew. Chem. Int. Ed.* 56 (2017) 13694–13698.
- [14] J. Su, Y. Yang, G. Xia, J. Chen, P. Jiang, Q. Chen, *Nat. Commun.* 8 (2017) 14969.
- [15] L. Zhu, H. Lin, Y. Li, F. Liao, Y. Lifshitz, M. Sheng, S. Lee, M. Shao, *Nat. Commun.* 7 (2016) 12272.
- [16] P. Jiang, Y. Yang, R. Shi, G. Xia, J. Chen, J. Su, Q. Chen, *J. Mater. Chem. A* 5 (2017) 5475–5485.
- [17] J. Mahmood, F. Li, S. Jung, M. Okyay, I. Ahmad, S. Kim, N. Park, H. Jeong, J. Baek, *Nat. Nanotechnol.* 12 (2017) 441–446.
- [18] Z. Xing, X. Yang, A.M. Asiri, X. Sun, *ACS Appl. Mater. Interfaces* 8 (2016) 14521–14526.
- [19] J. Tian, Q. Liu, A.M. Asiri, X. Sun, *J. Am. Chem. Soc.* 136 (2014) 7587–7590.
- [20] M.D. Segall, P.J.D. Lindan, M.J. Probert, C.J. Pickard, P.J. Hasnip, S.J. Clark, M.C. Payne, *J. Phys. Condens. Matter* 14 (2002) 2717–2744.
- [21] J.P. Perdew, K. Burke, M. Ernzerhof, *Phys. Rev. Lett.* 77 (1996) 3865–3868.
- [22] D.R. Hamann, M. Schlüter, C. Chiang, *Phys. Rev. Lett.* 43 (1979) 1494–1497.
- [23] D. Voiry, H. Yamaguchi, J. Li, R. Silva, D.C.B. Alves, T. Fujita, M.W. Chen, T. Asefa, V. Shenoy, G. Eda, M. Chhowalla, *Nat. Mater.* 12 (2013) 850–855.
- [24] Y. Liu, X. Xu, J. Zhang, H. Zhang, W. Tian, X. Li, M.O. Tade, H. Sun, S. Wang, *Appl. Catal. B: Environ.* 239 (2018) 334–344.
- [25] J. Liu, Y. Liu, D. Xu, Y. Zhu, W. Peng, Y. Li, F. Zhang, X. Fan, *Appl. Catal. B: Environ.* 241 (2019) 89–94.
- [26] Z. Xing, C. Han, D. Wang, Q. Li, X. Yang, *ACS Catal.* 7 (2017) 7131–7135.
- [27] Q. Gao, *Appl. Catal. B: Environ.* 235 (2018) 84–91.
- [28] Y. Yang, W. Zhang, Y. Xiao, Z. Shi, X. Cao, Y. Tang, Q. Gao, *Appl. Catal. B: Environ.* 242 (2019) 132–139.
- [29] C. Guo, L. Zhang, J. Miao, J. Zhang, C.M. Li, *Adv. Energy Mater.* 3 (2013) 167–171.
- [30] Q. Liu, J. Tian, W. Cui, P. Jiang, N. Cheng, A.M. Asiri, X. Sun, *Angew. Chem. Int. Ed.* 53 (2014) 6710–6714.
- [31] M.C. Acevedo, M.L. Stone, J.R. Schmidt, J.G. Thomas, Q. Ding, H. Chang, M. Tsai, J. He, S. Jin, *Nat. Mater.* 14 (2015) 1245–1251.
- [32] M.A. Al-Daous, *Catal. Commun.* 72 (2015) 180–184.
- [33] D. Li, R. Li, M. Lu, X. Lin, Y. Zhan, L. Jiang, *Appl. Catal. B: Environ.* 200 (2017) 566–577.
- [34] V.R. Surisetty, A.K. Dalai, J. Kozinski, *Appl. Catal. A: Gen.* 381 (2010) 282–288.
- [35] P. Betancourt, A. Rives, R. Hubaut, C.E. Scott, J. Goldwasser, *Appl. Catal. A: Gen.* 170 (1998) 307–314.
- [36] J. Zhang, T. Wang, D. Pohl, B. Rellinghaus, R. Dong, S. Liu, X. Zhuang, X. Feng, *Angew. Chem. Int. Ed.* 128 (2016) 6814–6819.
- [37] L. Shen, Q. Che, H. Li, X. Zhang, *Adv. Funct. Mater.* 24 (2014) 2630–2637.
- [38] H. Zhu, J. Zhang, R. Yanzhang, M. Du, Q. Wang, G. Gao, J. Wu, G. Wu, M. Zhang, B. Liu, J. Yao, X. Zhang, *Adv. Mater.* 27 (2015) 4752–4759.
- [39] X. Hao, Z. Jin, H. Yang, G. Lu, Y. Bi, *Appl. Catal. B: Environ.* 210 (2017) 45–56.
- [40] J. Xu, T. Liu, J. Li, Y. Liu, B. Zhang, D. Xiong, I. Amorim, W. Li, L. Liu, *Energy Environ. Sci.* 11 (2018) 1819–1827, <https://doi.org/10.1039/C7EE03603E>.
- [41] Z. Pu, I.S. Amiinu, Z. Kou, W. Li, S. Mu, *Angew. Chem. Int. Ed.* 56 (2017) 11559–11564.
- [42] D. Yoon, J. Lee, B. Seo, B. Kim, H. Baik, S. Joo, K. Lee, *Small* 13 (2017) 1700052.